crystals

MDPI

Article

Mueller Matrix Polarimetric Imaging Analysis of Optical Components for the Generation of Cylindrical Vector Beams

Guadalupe López-Morales [1], María del Mar Sánchez-López [1,2,*], Ángel Lizana [3], Ignacio Moreno [1,4] and Juan Campos [3]

1 Instituto de Bioingeniería, Universidad Miguel Hernández de Elche, Avda. Universidad s/n, 03202 Elche, Spain; guadalupe.lopez@umh.es (G.L.-M.); i.moreno@umh.es (I.M.)
2 Departamento de Física Aplicada, Universidad Miguel Hernández de Elche, Avda. Universidad s/n, 03202 Elche, Spain
3 Departamento de Física, Universitat Autònoma de Barcelona, 08193 Bellaterra, Spain; angel.lizana@uab.es (Á.L.); juan.campos@uab.es (J.C.)
4 Departamento de Ciencia de Materiales, Óptica y Tecnología Electrónica, Universidad Miguel Hernández de Elche, Avda. Universidad s/n, 03202 Elche, Spain
* Correspondence: mar.sanchez@umh.es; Tel.: +34-966658329

Received: 14 November 2020; Accepted: 15 December 2020; Published: 18 December 2020

Abstract: In this work, we performed a Mueller matrix imaging analysis of two commercial optical components usually employed to generate and manipulate vector beams—a radial polarizer and a liquid-crystal *q*-plate. These two elements generate vector beams by different polarization mechanisms—polarizance and retardance, respectively. The quality of the vector beams relies on the quality of the device that generates them. Therefore, it is of interest to apply the well-established polarimetric imaging techniques to evaluate these optical components by identifying their spatial homogeneity in diattenuation, polarizance, depolarization, and retardance, as well as the spatial variation of the angles of polarizance and retardance vectors. For this purpose, we applied a customized imaging Mueller matrix polarimeter based on liquid-crystal retarders and a polarization camera. Experimental results were compared to the numerical simulations, considering the theoretical Mueller matrix. This kind of polarimetric characterization could be very helpful to the manufacturers and users of these devices.

Keywords: vector beams; polarimetric imaging; radial polarizers; *q*-plates; liquid-crystal retarders; polarimetric camera

1. Introduction

Liquid crystals (LC) are employed in a myriad of photonic applications because of their unique electro-optic properties. While display applications are certainly the most popular ones, the development of LC-based photonic components, such as optical filters, switches, waveguides, spatial light modulators, and retarders, are essential to perform manipulation of light [1]. LC retarders are included in polarimetry systems, due to their variable optical retardance, upon application of a voltage, avoiding mechanical rotation of the mounts. Besides achieving automatic polarization control and reducing the instrumental error, its retardance value can be tuned as a function of wavelength, thus, extending polarimetry to a broad wavelength range [2].

Mueller matrix (MM) polarimetric imaging is a very powerful technique that is widely used nowadays in many different areas like astronomy [3], remote sensing [4], materials characterization [5] or biomedical applications [6], including improvement of fundus images for ophthalmic diagnoses [7].

MM polarimetry is deemed very useful to characterize optoelectronic polarization controlling devices. For instance, MM imaging of liquid-crystal-on-silicon (LCOS) displays was used to identify retardance inhomogeneities [8] or depolarization caused by flicker [9]. MM imaging was applied to evaluate liquid-crystal variable retarders (LCR), where it proved very valuable to reveal non-ideal responses that might significantly affect their performance in advanced optical instruments [10,11]. It was also employed to test the performance as depolarizers of liquid-crystal (LC) cells for improving holographic systems [12].

In this work, using MM imaging analysis, we examined two commercial polarization devices employed to generate cylindrical vector beams (CVB)—a radial polarizer and two static q-plates. Such two kind of devices are capable of generating CVBs in compact and efficient optical setups, as opposed to other methods based on spatial light modulators, which, however, are more versatile [13].

CVBs are light beams with a spatially-variant state of polarization exhibiting axial symmetry, which are prompting advances in areas such as microscopy, materials processing, metrology, and optical classical and quantum communications [13–15]. Due to their inhomogeneous polarization pattern, they were also studied to develop snapshot polarimeters [16] and to test the performance of real-time Stokes polarimeters [17]. Radially and azimuthally polarized beams are the most common cases of CVBs. Early examples of radial and azimuthal beams were obtained using the twisted nematic LC cell reported in [18]. Further developments in photo-alignment techniques led to the current q-plate technology [19].

Q-plates are spatially-varying waveplates, typically of half-wave retardance, whose optical axis follows q times the azimuthal angle θ. They convert input linearly polarized light into a CVB, whose order ($m = 2q$) is given by the device q-value [20]. Since they impart a helical phase $\exp(\pm i2q\theta)$ on input circularly polarized light, they are widely used to generate and manipulate vortex beams (light beams with Orbital Angular Momentum, OAM), which is crucial in quantum communications [19]. Q-plates can be fabricated with LC materials [21], or by patterning subwavelength structures in non-birefringent materials like silica glass [22] (so-called metamaterial q-plates or s-plates). In all cases, the q-value is set on fabrication and cannot be changed. In polymer LC and in metamaterial q-plates, the retardance at the operation wavelength is set on fabrication; they are static plates. Most commercial q-plates are of this kind [23]. When fabricated with nematic LC and with transparent electrodes, the q-plate retardance can be tuned by an applied voltage and the operation wavelength can cover the VIS and NIR range [24]. Retardance tunability is very useful in order to manipulate vector beams, since it controls the polarization conversion efficiency [19], which is maximum for half-wave retardance. However, the capability of generating hybrid vector beams, from standard to more exotic ones, using q-plates tuned at quarter-wave retardance is also shown [22,25].

Another simple method to generate CVBs is by using a radial polarizer and waveplate combinations [26]. Actual radial polarizers are patterned devices consisting of angular sectors made of linear polarizers, where the transmission axis is oriented in each sector, along the corresponding radial direction. By illuminating it with either unpolarized light or with circularly polarized light, the output beam is radially polarized. This radial polarization can then be converted into azimuthal polarization, just by placing a polarization rotator composed of two half-wave plates (HWP). Other spatial polarization patterns with axial symmetry can be generated by using combinations of HWPs and quarter-wave plates (QWP) [26].

Radial polarizers and q-plates are usually analyzed in terms of Jones matrices because they are assumed to operate with fully polarized light. Fabricated birefringent components are usually tested using a quantitative birefringence measurement equipment that typically includes an optical microscope. In this way, the retardance value distribution and the local optical axes variation can be measured [22]. However, the MM approach provides additional general information about relevant parameters like depolarization, diattenuation, polarizance, and retardance. In the specific case of q-plates, it is necessary to determine the spatial orientation of its optical axis and the spatial homogeneity of the retardance value. In the case of the radial polarizer, it is necessary to determine the spatial

distribution of the transmission axis and the spatial homogeneity of the polarizance. The Lu-Chipman decomposition of the measured MM [27] is applied to achieve these parameters. Therefore, in this work we propose the MM polarimetric characterization as an additional tool for testing the quality of these devices, which can be helpful to manufacturers and users.

This paper is organized as follows. After this Introduction, in Section 2 we summarize the theoretical Mueller–Stokes formalism to describe CVBs and derive the MM of the radial polarizer and the q-plate. Section 3 presents the experimental arrangement of our imaging polarimeter. We employed a Liquid Crystal–Polarization State Generator (LC–PSG) whose calibration was reported in [28]. A polarization camera that simultaneously analyzes the four cardinal linear polarizations was used as Polarization State Analyzer (PSA), together with a movable QWP. This arrangement lowered the required number of measurements to only twelve PSG–PSA configurations. The imaging MM results of the radial polarizer and the q-plates are given in Section 4. The experimental results are compared to numerical simulations, and their physical interpretation is discussed. The polarization map of the CVBs generated with each device upon illumination with circularly polarized light is shown. The conclusions of this study are summarized in Section 5.

2. Materials and Methods

As mentioned, CVBs and the two devices (radial polarizer and q-plates) employed here for their generation are usually treated within the Jones matrix formalism, since fully polarized light is considered. However, since here we are applying am MM polarimeter, next we briefly review them within the Mueller–Stokes formalism and provide the required framework for this MM analysis.

2.1. Vector Beams in the Stokes formalism

A fully polarized state of polarization can be described by the Stokes parameters $\mathbf{S}^T = (1, \cos(2\varepsilon)\cos(2\Psi), \cos(2\varepsilon)\sin(2\Psi), \sin(2\varepsilon))$ where T denotes the transposed matrix and ε and Ψ are the ellipticity and azimuthal angles of the polarization ellipse, respectively [29]. Therefore, the Stokes parameters of a vector beam (S_{VB}) can be simply obtained by setting the dependence of Ψ on the azimuthal coordinate (θ) as $\Psi = \ell\theta + \Psi_0$, where ℓ is the topological charge of the CVB and Ψ_0 is the orientation of the polarization state at the azimuth origin $\theta = 0$, i.e.,

$$\mathbf{S}_{VB} = \begin{pmatrix} 1 \\ \cos(2\varepsilon)\cos(2\ell\theta + 2\Psi_0) \\ \cos(2\varepsilon)\sin(2\ell\theta + 2\Psi_0) \\ \sin(2\varepsilon) \end{pmatrix}. \tag{1}$$

Figure 1 illustrates some examples of order $\ell = 1$, where the radial and the azimuthal vector beams are typical cases, given respectively, by $\Psi_0 = 0$ and $\Psi_0 = \pi/2$, and $\varepsilon = 0$. Their corresponding radial and azimuthal Stokes parameters are given by:

$$\mathbf{S}_{Radial} = \begin{pmatrix} 1 \\ \cos(2\theta) \\ \sin(2\theta) \\ 0 \end{pmatrix}, \ \mathbf{S}_{Azimuthal} = \begin{pmatrix} 1 \\ -\sin(2\theta) \\ \cos(2\theta) \\ 0 \end{pmatrix}. \tag{2}$$

Let us note that ε is a constant angle that describes the ellipticity of the polarization state, which remains constant in the transversal plane, whereas the orientation of the ellipse changes with θ, as shown in Figure 1d. Depending on the ε and Ψ values in Equation (1), it is possible to generate different vector beams. Although other types of CVBs exist, we restrict the analysis to these standard CVBs, since they are directly generated with the radial polarizer and the q-plates.

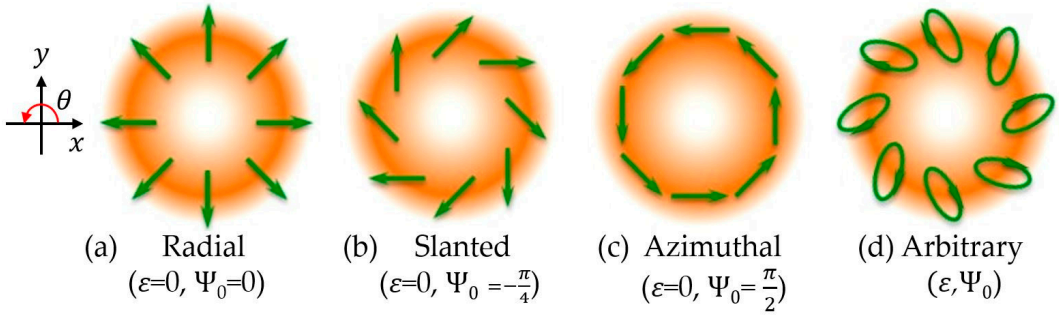

Figure 1. Different kinds of vector beams of order $\ell = 1$. (**a**) Radial (**b**) Slanted (**c**) Azimuthal (**d**) Arbitrary.

2.2. Mueller Matrix of an Ideal Radial Polarizer and an Ideal Q-Plate

Next, we describe the two kinds of optical devices considered in this work—a radial polarizer from CODIXX [30] and two static polymer LC q-plates from Thorlabs with $q = 1$ (model WPV10-633) and $q = 1/2$ (model WPV10L-633) [31]. We include analytical expressions of their Mueller matrices, which are not encountered in works on vector beams that most often use the Jones formalism. As shown in Figure 2, the most characteristic feature of these devices is the azimuthal orientation of the transmission axis (radial polarizer, Figure 2d) and of the optical axis (q-plates, Figure 2e,f). The q-plate of $q = 1/2$ has a mark in its mount that indicates the zero-degree optical axis, which we have aligned in the x-axis orientation, as shown in Figure 2f.

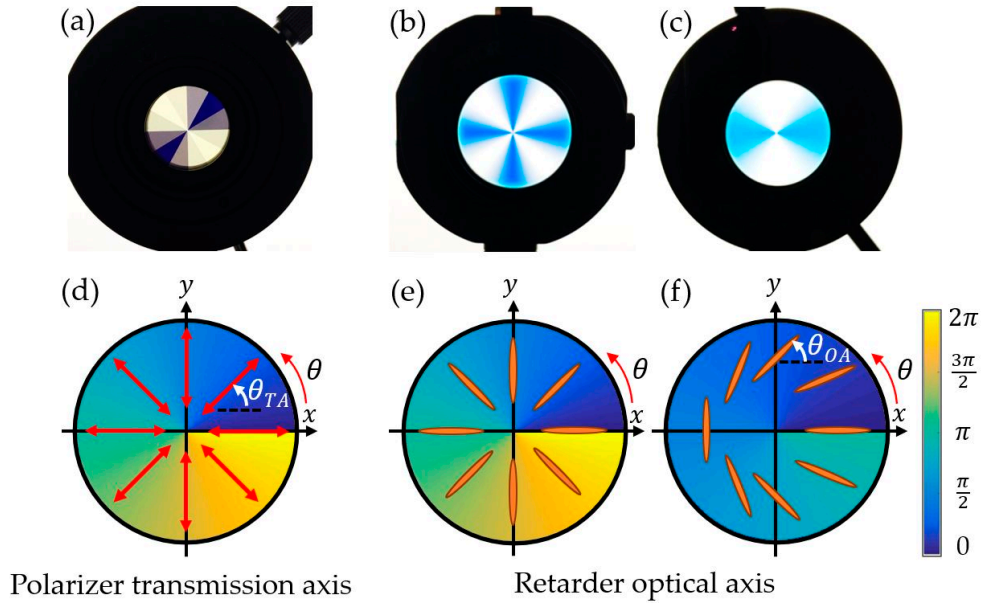

Figure 2. (**a**) Photograph of the radial polarizer under broadband linearly polarized light. Photographs of the q-plates with (**b**) $q = 1$ and (**c**) $q = 1/2$ placed between linear parallel polarizers and under broadband illumination. (**d**) Azimuthal orientation of the transmission axis of the radial polarizer. Azimuthal orientation of the optical axis of the q-plate with (**e**) $q = 1$ and (**f**) $q = 1/2$. The color code indicates the orientation angle of these axis.

The top row in Figure 2 shows a photograph of each device under broadband illumination with linearly polarized light. In the case of the q-plates, a linear analyzer (parallel to the input polarization) was placed before the camera in order to visualize the azimuthal variation. In the case of the radial polarizer, the intensity azimuthal variation is directly observed when illuminating with linear polarizer light. The diameter of the radial polarizer was 2 cm, while the q-plates diameter was one inch. Figure 2a

clearly reveals the segmented nature of the CODIXX polarizer, with 12 segments of fixed transmission axis orientation. On the contrary, we can see in Figure 2b,c that these q-plates are continuous devices (their optical axis linearly follows the azimuthal angle as $q\theta$). These photographs display the expected four-lobe and two-lobe intensity pattern of q-plates with $q = 1$ (Figure 2b) and $q = 1/2$ (Figure 2c). Note also their birefringence colors, which can be used to estimate the device retardance [32]. The radial polarizer (Figure 2a) does not exhibit such colors because it is effective in a wide spectral range that covers the full visible spectrum.

2.2.1. Radial Polarizer

The radial polarizer (Figure 2a) produces a light beam with a radial transverse spatial distribution of the polarization state [14,26]. The ideal MM describing it reads:

$$\mathbf{M}_{RP} = \frac{1}{2}\begin{pmatrix} 1 & \cos(2\ell\theta) & \sin(2\ell\theta) & 0 \\ \cos(2\ell\theta) & \cos^2(2\ell\theta) & \sin(2\ell\theta)\cos(2\ell\theta) & 0 \\ \sin(2\ell\theta) & \sin(2\ell\theta)\cos(2\ell\theta) & \sin^2(2\ell\theta) & 0 \\ 0 & 0 & 0 & 0 \end{pmatrix}. \tag{3}$$

This is the Mueller matrix for a linear polarizer [29], where now the angle of the transmission axis is $\theta_{TA} = \ell\theta$. The standard radial polarizer has $\ell = 1$. Note that for input non-polarized light $\mathbf{S}_{in}^T = (1, 0, 0, 0)$ and for input circularly polarized light $\mathbf{S}_{in}^T = (1, 0, 0, \pm 1)$ the output Stokes parameters $\mathbf{S}_{out} = \mathbf{M}_{RP} \cdot \mathbf{S}_{in}$ correspond to the radial beam of order $\ell = 1$ in Equation (2).

2.2.2. Q-Plates

Radially polarized light can also be generated by a q-plate [19]. As mentioned, it consists of a spatially variable linear retarder with a phase-shift (linear retardance) and optical axis orientation ($\theta_{OA} = q\theta + \alpha_0$) that rotates a fraction q of the azimuthal angle θ, and α_0 is the offset angle, i.e., the orientation angle of the optical axis at $\theta = 0$. Figure 2e,f illustrate the case of $q = 1$ and $q = 1/2$, where the optical axis at given angles is depicted as brown ellipses and the colored background indicates the continuous distribution of the optical axis. For $q = 1$, the optical axis rotates through $[0 - 2\pi]$, whereas for $q = 1/2$ it only rotates π radians.

The MM for the ideal q-plate is:

$$\mathbf{M}_q(\phi) = \begin{pmatrix} 1 & 0 & 0 & 0 \\ 0 & \cos^2(2q\theta) + \cos(\phi)\sin^2(2q\theta) & (1 - \cos(\phi))\sin(2q\theta)\cos(2q\theta) & -\sin(\phi)\sin(2q\theta) \\ 0 & (1 - \cos(\phi))\sin(2q\theta)\cos(2q\theta) & \sin^2(2q\theta) + \cos(\phi)\cos^2(2q\theta) & \sin(\phi)\cos(2q\theta) \\ 0 & \sin(\phi)\sin(2q\theta) & -\sin(\phi)\cos(2q\theta) & \cos(\phi) \end{pmatrix}. \tag{4}$$

where we consider with $\alpha_0 = 0$ for simplicity. The MM in Equation (4) was equivalent to that of a linear retarder with retardance and variant orientation $\theta_{OA} = q\theta$ [29]. In the standard case of a half-wave (HW) q-plate with $\phi = \pi$, the MM is given by:

$$\mathbf{M}_q(\phi = \pi) = \begin{pmatrix} 1 & 0 & 0 & 0 \\ 0 & \cos(4q\theta) & \sin(4q\theta) & 0 \\ 0 & \sin(4q\theta) & -\cos(4q\theta) & 0 \\ 0 & 0 & 0 & -1 \end{pmatrix}. \tag{5}$$

Now, if the input beam is horizontally or vertically linearly polarized, $\mathbf{S}_{in}^T = (1, \pm 1, 0, 0)$, the output Stokes parameters, $\mathbf{S}_{out} = \mathbf{M}_q(\phi = \pi) \cdot \mathbf{S}_{in}$ respectively correspond to the radial and to the azimuthal vector beams in Equation (2) for the q-plate with $q = 1/2$.

These devices, however, can also be operated at detuned retardance. In this work, we use a retardance of $\phi = 3\pi/2$ and the device can be regarded as a spatially-variable QWP [33]. The MM for such QW q-plate reads:

$$\mathbf{M}_q(\phi = \frac{3}{2}\pi) = \begin{pmatrix} 1 & 0 & 0 & 0 \\ 0 & \cos^2(2q\theta) & \sin(2q\theta)\cos(2q\theta) & \sin(2q\theta) \\ 0 & \sin(2q\theta)\cos(2q\theta) & \sin^2(2q\theta) & -\cos(2q\theta) \\ 0 & -\sin(2q\theta) & \cos(2q\theta) & 0 \end{pmatrix}. \tag{6}$$

In this case, the linearly polarized vector beam is obtained when the device is illuminated with input circular polarization [22]. For instance, by applying Equation (6) on input right-handed circular polarization $\mathbf{S}_{in}^T = (1, 0, 0, 1)$ one obtains an output that corresponds to the slanted vector beam in Figure 1b. Note that in this QW q-plate situation, the generated vector beam is of order $\ell = q$, in contrast to the standard case with the HW q-plate that provides CVBs of $\ell = 2q$ [33].

2.3. Mueller Matrix Decomposition

In this work, we applied the Lu-Chipman decomposition [27] to the measured MM in order to obtain the polarization parameters of interest. This decomposition is summarized here and the details of the calculation are provided in Appendix A.

The Lu-Chipman decomposition describes an MM as the product of three matrices:

$$\mathbf{M} = \mathbf{M}_\Delta \cdot \mathbf{M}_R \cdot \mathbf{M}_D. \tag{7}$$

which provides the diattenuation $\mathbf{M}_D$, retardance $\mathbf{M}_R$, and depolarization $\mathbf{M}_\Delta$ properties of the sample. This equation is written explicitly as:

$$\mathbf{M} = m_{00} \begin{bmatrix} 1 & \vec{0}^T \\ \vec{\mathbf{P}}_\Delta & \mathbf{m}_\Delta \end{bmatrix} \cdot \begin{bmatrix} 1 & \vec{0}^T \\ \vec{0} & \mathbf{m}_R \end{bmatrix} \cdot \begin{bmatrix} 1 & \vec{\mathbf{D}}^T \\ \vec{\mathbf{D}} & \mathbf{m}_D \end{bmatrix}. \tag{8}$$

where $\vec{\mathbf{D}}$ is the diattenuation vector, $\vec{\mathbf{P}}_\Delta$ is the polarizance vector of the depolarizer part, $\mathbf{m}_\Delta$, $\mathbf{m}_R$ and $\mathbf{m}_D$ are the 3×3 submatrices of $\mathbf{M}_\Delta$, $\mathbf{M}_R$, $\mathbf{M}_D$, and $\vec{0}^T = [0\,0\,0]$.

Note that the multiplication of these matrices is not commutative, therefore, the result depends on the order of how they are multiplied [27,34], and other approaches could be applied, as the reverse product decomposition [35], among others. In this work, we choose the Lu-Chipman decomposition, Equations (7) and (8), as it is the most commonly used approach in polarimetric applications and we observed that it properly describes the physical response of the studied components. Although our samples are ideally either a pure polarizing element (radial polarizer) or a pure retarder element (q-plates), we consider this general decomposition to avoid any apriorism.

We note that the decomposition must follow two different calculations, depending on whether the diattenuation matrix $\mathbf{M}_D$ is singular or not. Appendix A describes the full procedure and the equations used for the polarimetric parameters. As a result of this decomposition, the next sections include imaging results of the measured diattenuation (D), polarizance (P), depolarization (Δ), and retardance (R) parameters, as well as the spatial map that describes the orientation of the transmission axis (for the radial polarizer) and of the principal axis (for the q-plates).

3. Experimental Arrangement of the Mueller Matrix Polarimeter

In this section, we describe the optical system of our imaging MM polarimeter shown in Figure 3. As light source, we use the 488 nm line of an air-cooled Ar-Kr laser (CVI/Melles Griot, Mod. 35-LTL-835-240, Albuquerque, NY, US). A spatial filter, consisting of a 20× microscope objective (Newport, M-20×, North Logan, UT, US) and a pinhole aperture (Newport, 900PH15, North Logan, UT,

US) of 15 µm diameter cleans up the light beam, which is then collimated by a lens L1 (f_1 = 75 mm). The LC-PSG is built by a linear polarizer (Thorlabs, LPVISE200A) with its transmission axis (TA) in the vertical direction, followed by two liquid–crystal variable retarders (LCR) from ArcOptix [36], oriented at 45° and 90°, respectively, and a QWP (Thorlabs, AQWP05M600, Newton, NJ, US) with its fast axis (FA) at −45°. The two commercial LCRs employed were calibrated at 488 nm wavelength and their retardance curve as a function of voltage, $\phi_1(V)$ and $\phi_2(V)$ were obtained. These curves and the driving voltage values of LCR1 and LCR2 that were required to generate the six standard states of polarization—horizontal (H), vertical (V), ±45° linear polarizations, and right- (RCP) and left-handed (LCP) circular polarizations, are given in [28]. The polarization state analyzer (PSA) consists of a second QWP (Thorlabs, WPQ05M488, Newton, NJ, US) with its FA vertically oriented and a Kiralux™ Polarization Camera (Thorlabs, CS505MUP, Newton, NJ, US). This camera has a monochrome CMOS Sensor of 5 megapixels with a wire grid polarizer array that consists of a repeating pattern of polarizers with their transmission axes at 0°, 45°, −45°, and 90°. Therefore, QWP2 is only placed in the PSA when the circular polarization states need to be analyzed. The sample is placed between the LC-PSG and the PSA, and the sample plane is imaged on the camera by a second lens L2 (f_2 = 150 mm).

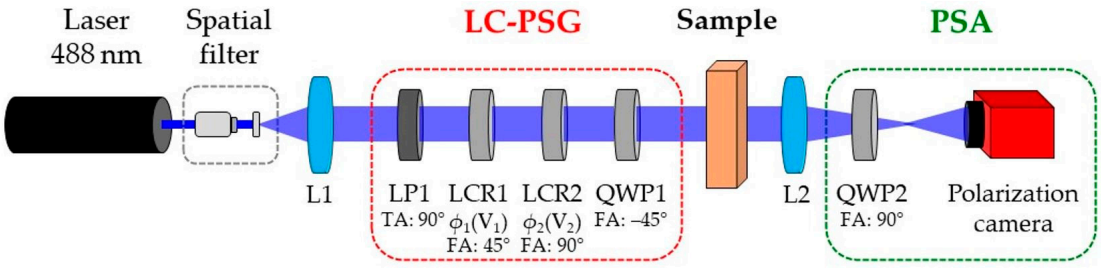

Figure 3. Schematic representation of the Mueller matrix polarimeter (L: lens, LP: linear polarizer, LCR: liquid-crystal retarder, QWP: quarter-wave plate).

To obtain the experimental MM, a set of six standard polarization states is generated by the LC–PSG and analyzed by the PSA. Let us remark that our polarization camera analyzes in a single shot the four linear states of polarization (H, V, +45°, and −45°), thus, lowering the number of actual measurements to only 12 different PSG–PSA configurations. The LC–PSG system in reverse order followed by a digital camera could also perform as an LC–PSA, but it would require measuring 36 configurations [28]. Certainly, most convenient would be using a commercial imaging MM polarimeter [37], but these instruments are usually quite expensive. Thus, the MM polarimeter system developed in this work is a good alternative since it performs measurements with good accuracy at an affordable cost. The elements of the imaging MM are calculated according to [38], where we first verified the correct calibration of our polarimeter, by measuring the MM of air, which is an identity matrix, and other known elements such as linear polarizers and waveplates, with relative errors less than 7% for the MM coefficient measurements. Performing the same experimental procedure, we obtain the MM image of the radial polarizer and the *q*-plates. In the calibration of the polarimeter, we detected an interference pattern produced by the interaction of the coherent source with the LCRs [39], in addition to the possible multiple reflected beams between the optical components. Therefore, a digital Notch filter is applied to the intensity images captured by the camera, to eliminate this periodic noise [40].

In the next section, we discuss the MM imaging results obtained for these devices. Such analysis relies, notwithstanding, on the accuracy of the imaging polarimetry system. Note that our system in Figure 3 is devoid of moving or rotating elements, with the exception of QWP2, which must be placed when analyzing the circular polarizations. This could be avoided by placing a third LCR with addressable voltage in front of the polarization camera. Therefore, the placing and removing of QWP2 might cause image errors, such as the beam wander effect [41]. Other possible experimental errors can be due to slight misalignment of the optical components, laser speckle, and noise in the camera itself. Nevertheless, the results shown in the following section reveal a good accuracy of our polarimeter.

4. Results and Discussion

4.1. Imaging Mueller Matrix Results of the Radial Polarizer

First, we show the experimental and numerical MM images of the radial polarizer and the main optical properties of the device obtained from its analysis. Figure 4 illustrates the normalized MM of the segmented radial polarizer. Figure 4a represents the numerical ideal MM obtained from Equation (3). Our simulation considers the segmentation of the CODIXX polarizer. That is, the numerical calculation of the MM in Equation (3) considers 12 angular sectors, where the transmission axis rotates with the azimuthal coordinate but keeps a fixed orientation within each sector. Of course, the physical border between segments cannot be accounted for in these simulations and will only appear in the experimental results. Note the following symmetries of the MM elements as corresponding to a linear polarizer: $m_{01} = m_{10}$, $m_{02} = m_{20}$, $m_{03} = m_{30}$, $m_{12} = m_{21}$, and $m_{11} = 1 - m_{22}$. Note that the three first equalities lead to $\vec{\mathbf{D}} = \vec{\mathbf{P}}$, and these optical components present the same diattenuation response independently, if they are measured in the backward or forward direction [42].

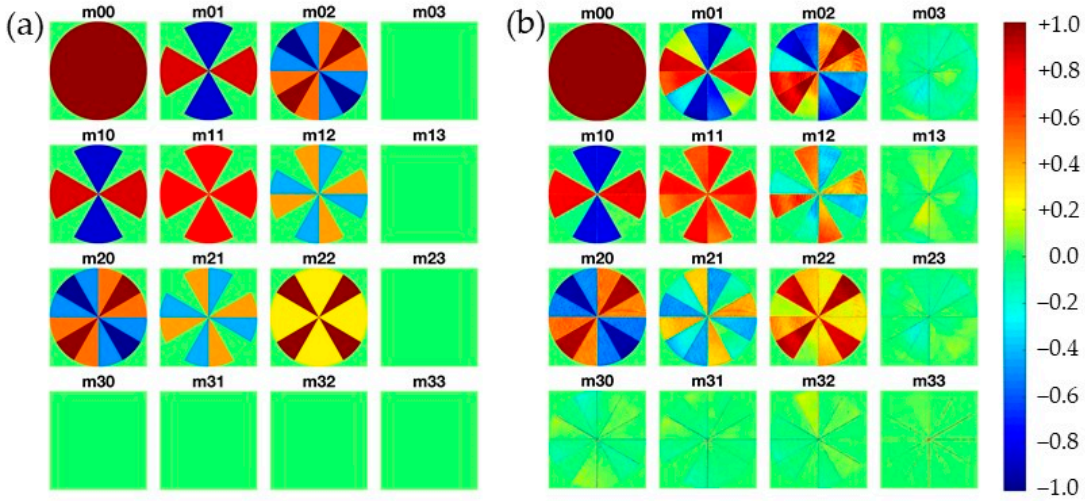

Figure 4. Normalized MM of the radial polarizer. (**a**) Ideal numerical MM (Equation (3)), and (**b**) experimental measure.

The experimental MM is shown in Figure 4b. It holds very good agreement with the numerical one. A certain amount of noise is apparent in the elements of the last row and column of the MM in Figure 4b. Element m_{03} presents the maximum absolute error averaged in the whole area (0.11). The absolute error is 0.22 when averaged over 60×60 pixels in the blue region in m_{03}. Note that the borders between the segments of the radial polarizer are clearly observed in the images of the bottom row of Figure 4b, particularly in element m_{33}. This means that our polarimetric system is very sensitive in detecting details in the sample. These results are comparable to those reported for a radial polarizer patched with eight sectors [43].

From the elements of the first row and column of the MM of Figure 4, the diattenuation (D) and polarizance (P) parameters are directly calculated and plotted pixel-by-pixel, using Equation (A2). Let us recall that elements m_{01} and m_{02} in the experimental images in Figure 4b are not identical to elements m_{10} and m_{20}. Hence, we cannot expect parameters D and P to take exactly the same value in our experimental results, as it occurs in the ideal numerical calculation. The diattenuation parameter describes the intensity transmittance capability to the polarized light [29]; therefore, a similar experimental D value would be expected on the entire surface. The experimental diattenuation image of the radial polarizer illustrated in Figure 5(b1) allows to visualize the segmentation of this device, as well as the slight variation between segments. For instance, segment #3 presents the greatest diattenuation value with $D = 0.957$ while segment #11 shows the least one with $D = 0.831$. Although it

is possible to observe a different shade of red between the segments, the average value on the whole surface is $D = 0.909$, with a standard deviation of ±0.018. Hence, the radial polarizer presents a good homogeneity on its surface for this parameter.

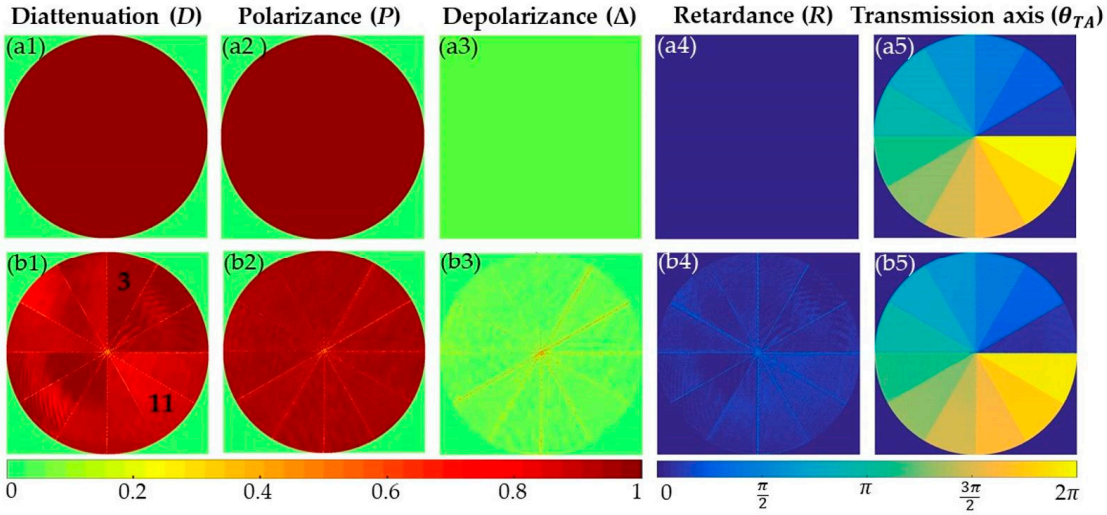

Figure 5. Polarimetric parameters of the radial polarizer. (**a1**–**a5**) Ideal numerical and (**b1**–**b5**) experimental measure of diattenuation, polarizance, depolarizance, retardance, and transmission angle.

The polarizance parameter shows the degree of polarization in transmitted light when unpolarized light strikes the sample, i.e., it provides the capability of a sample to polarize an unpolarized beam [29]. Figure 5(a2) corresponds to the numerical polarizance for an ideal polarizer, where each pixel is $P = 1$ and compares with Figure 5(b2) that shows the experimental polarizance for the radial polarizer. The average polarizance on the whole surface and its standard deviation is $P = 0.944 \pm 0.013$. Thus, the capability to polarize light is almost uniform on the whole device.

Since the diattenuation MM of the radial polarizer is singular, the MM decomposition must follow the procedure described in Appendix A, and the depolarization parameter (Δ) is calculated by Equation (A6). The ideal depolarization image should be $\Delta = 0$, as in Figure 5(a3), since it is a polarizing device. The experimental depolarization image is shown in Figure 5(b3). The average experimental value and its standard deviation is $\Delta = 0.056 \pm 0.013$, which indicates that the surface of this device can be considered homogeneous. Only at the borders between the segments, the value is significantly higher and are clearly visible, with an average value of $\Delta = 0.15 \pm 0.04$ on the border between segments #2 and #3. This can be attributed to the spatial averages conducted at the edges of the segments due to the CCD pixel size.

The retardance (R) parameter is obtained from Equation (A5). The experimental average retardance value and standard deviation in Figure 5(b4) is $R = 0.07\pi \pm 0.01\pi$. This value is consistent, within the experimental error, with the expected null retardance of a perfect polarizer (Figure 5(a4)). The MM decomposition also allows us to determine the orientation of the transmission axis (θ_{TA}) of a polarizing element, using Equation (A7). The simulation and the experimental results are compared in Figure 5(a5,b5). The angular values lie in the range $[0 - 2\pi]$. The experimental angle values for each segment of the radial polarizer bear an excellent agreement with the expected values.

4.2. Imaging Mueller Matrix Results of the q-Plate

Let us describe the polarimetric response of the q-plates of $q = 1$ and $q = 1/2$. Previous calibrations indicate that they have a retardance value very close to $\phi = 3\pi/2$ at 488 nm [33]. The numerical MM of the q-plates of $q = 1$ and $q = 1/2$ are obtained by using Equation (6); they are shown in Figure 6a,c, respectively. In this case, the symmetry conditions of their MM elements are $m_{12} = m_{21}$, $m_{13} = -m_{31}$, $m_{23} = -m_{32}$, and $m_{11} = 1 - m_{22}$. Except for m_{00}, the first row and column of the MM

image are null, i.e., $\vec{\mathbf{D}} = \vec{\mathbf{P}} = \vec{0}$, as corresponds to pure retarder systems. Following the previous experimental procedure, the experimental MM are obtained for both q-plates of $q = 1$ and $q = 1/2$, which are shown in Figure 6b,d, respectively. The experimental MM are consistent with the numerical ones and the symmetry conditions hold very well. The maximum average absolute error, attributable to the experimental noise is 0.14 and occurs in element m_{33}. The number of lobes in the Mueller matrix elements depends on the order of the q-plate. For instance, element for m_{11} the q-plate with $q = 1$ has four lobes, while for $q = 1/2$ it only has two lobes.

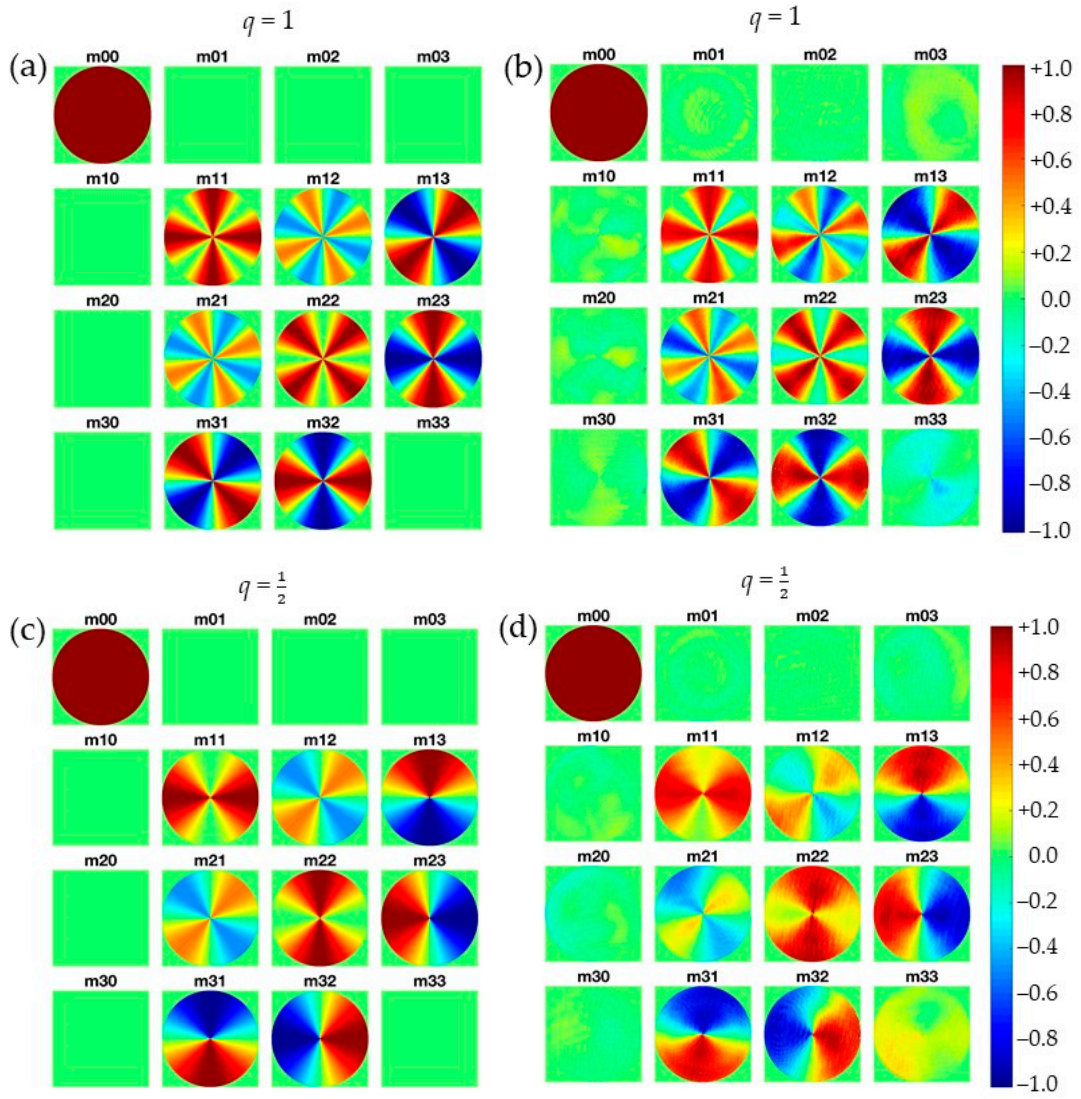

Figure 6. Normalized MM of the q-plate of $q = 1$ (first row) and $q = 1/2$ (second row). (**a**,**c**) Ideal numerical MM (Equation (6)) and (**b**,**d**) experimental measure.

Diattenuation and polarizance are calculated directly from the MM using Equation (A2), but to know the rest of optical properties, it is necessary to apply the decomposition that is explained in Appendix A. Their diattenuation MM are not singular, therefore to determine the depolarization and retardance parameters, we applied Equations (A11) and (A12b), respectively. The numerical results for both q-plates are similar. Therefore, we only compare the numerical and experimental polarimetric parameters for the q-plate with $q = 1$ in Figure 7. The experimental results for the q-plate with $q = 1/2$ are shown in Figure 8.

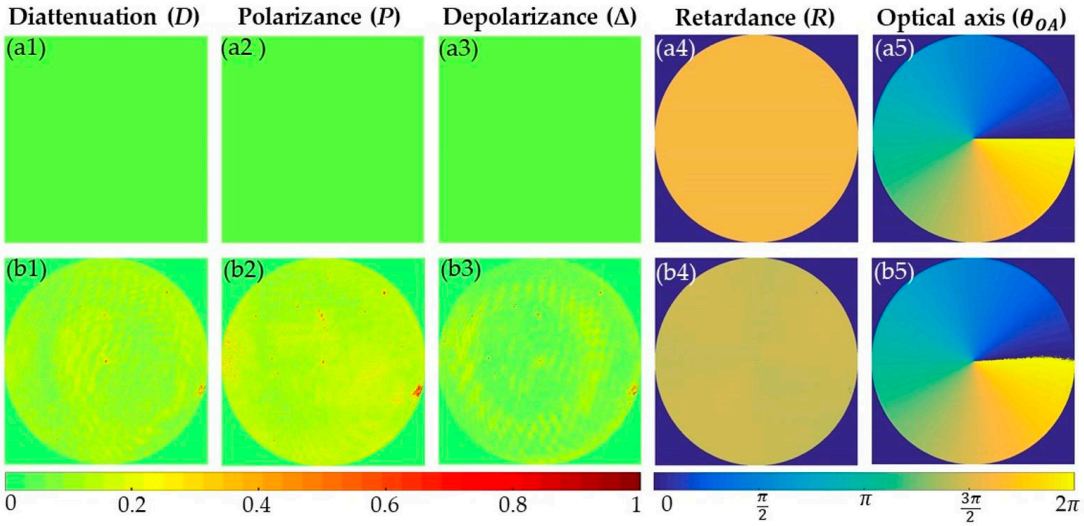

Figure 7. Polarimetric parameters of the q-plate with $q = 1$. (**a1**–**a5**) Numerical and (**b1**–**b5**) experimental measure.

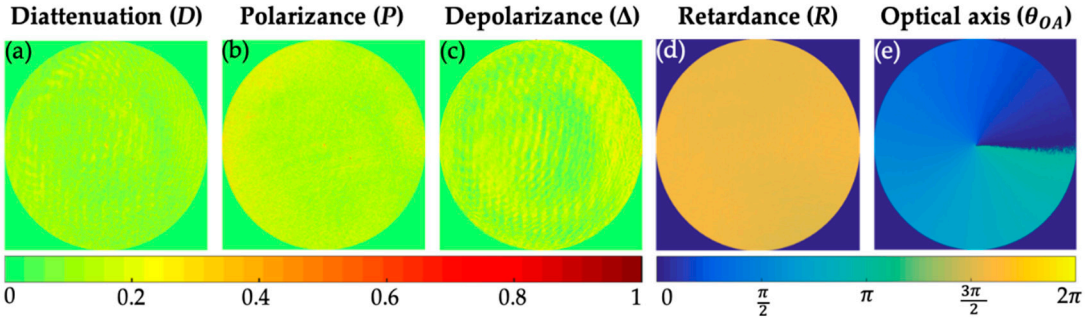

Figure 8. Experimental polarimetric parameters of the q-plate with $q = 1/2$. (**a**) Diattenuation, (**b**) polarizance, (**c**) depolarizance, (**d**) retardance, and (**e**) orientation of the optical axis.

As expected, the diattenuation (D), polarizance (P), and depolarization (Δ) values of an ideal q-plate are null, as shown in Figure 7(a1–a3), respectively. The non-null experimental values of parameters D, P, and Δ for the q-plate with $q = 1$ (Figure 7(b1–b3)), and $q = 1/2$ (Figure 8a–c), agree well within the margins of the experimental error of the experimental system.

The average value and standard deviation of each parameter for the q-plate with $q = 1$, in Figure 7(b1–b3), were calculated with the aim of analyzing the homogeneity of this device, giving the following results: $D = 0.108 \pm 0.007$, $P = 0.139 \pm 0.007$, and $\Delta = 0.043 \pm 0.006$. Since the values of the standard deviation are small, this means that this q-plate has uniformity over its entire surface.

The analysis of the retardance (R) parameter is essential for the q-plates due to the retarder nature of these devices. Figure 7(a4) corresponds to the numerical result for q-plate with $q = 1$. The experimental retardance image, shown in Figure 7(b4), yields a mean value of $R = 1.45\pi$ with a standard deviation of $\pm 0.05\pi$, which indicates that this device is homogeneous. This result is in good agreement with the previous spectral characterization of this q-plate [33], which indicated a phase-shift of $\phi = 3\pi/2$ for the wavelength of 475 nm, very close to the 488 nm wavelength used in the measurements in Figure 7.

The characteristic null intensity at the center of the beam caused by the vortex generated by the q-plate was hardly visible at the center of the images of P, D, Δ, and R because the camera was placed at the position where it captured the image of the device. By slightly moving the camera, the vortex null intensity becomes visible as a spot in the center.

The retardance vector was calculated from Equation (A13) and the direction of the device optical axis (θ_{OA}) was given by Equation (A14). The distribution of θ_{OA} for the q-plate of $q = 1$ goes continuously from 0 to 2π radians, with good agreement between the numerical (Figure 7(a5)) and the

experimental (Figure 7(b5)) results. The experimental images for the q-plate with $q = 1/2$ of parameters D, P, and Δ are illustrated in Figure 8a–c, respectively. Their mean value and standard deviation were: $D = 0.106 \pm 0.004$, $P = 0.136 \pm 0.005$, and $\Delta = 0.119 \pm 0.005$. The retardance image for the q-plate of $q = 1/2$ is shown in Figure 8d. The average value was $R = 1.555\pi$ with a standard deviation of $\pm 0.005\pi$, which indicated a good homogeneity. On the other hand, the rotation of the optical axis reached only up to $\theta_{OA} = \pi$ upon performing the cycle of $\theta \in [0, 2\pi)$, as shown in Figure 8e. While the axis orientation of the q-plate of $q = 1$ is indistinct due to its radial symmetry, for $q = 1/2$, it is necessary to know the offset angle, i.e., the orientation where the optical axis is aligned at zero-degree. Knowing the offset angle is crucial because it determines the spatial polarization pattern that exits the device for a given input polarization and retardance [20].

4.3. Polarization Map of the CVBs Generated by the Radial Polarizer and the q-Plates

Finally, let us show the performance of these three optical components in generating CVBs. As mentioned in the Introduction, CVBs are finding many applications in areas like microscopy, laser microfabrication, and optical communications [13,14]. In all these applications, it is very convenient to obtain a clear visualization of the polarization pattern in order to verify how accurately the vector beam was generated. A polarization map plots the polarization ellipse of light at every pixel of the image. The MM imaging polarimetric results obtained in the previous section provides the values of the output Stokes parameters necessary to draw the polarization maps.

Figure 9 shows the experimental polarization maps of CVBs generated with the three devices used in this work. In the three cases we consider illumination with right circularly polarized light of wavelength 488 nm. From the experimental output Stokes parameters (S_{VB}) the polarization map of each vector beam was retrieved and the results are shown in Figure 9. The images show the calculated polarization ellipses drawn on the captured intensity image. The radial polarizer produces a radial beam of order $\ell = 1$, which is shown in Figure 9a. On the other hand, the q-plates generate a slanted beam of order $\ell = q$, where Figure 9b,c correspond to the q-plate of $q = 1$ and $q = 1/2$, respectively.

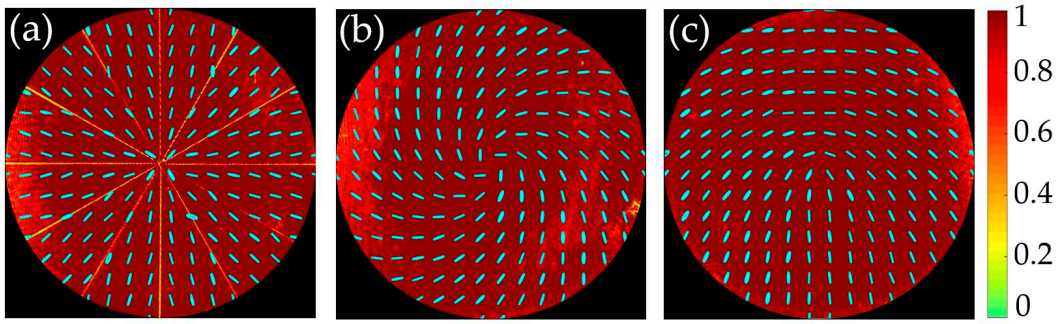

Figure 9. Experimental polarization map of the CVBs generated by (**a**) the radial polarizer and the q-plate with (**b**) $q = 1$ and (**c**) $q = \frac{1}{2}$, when the input beam is RCP light. The background color corresponds to the values of the Stokes parameter S_0. The drawn polarization ellipses are obtained from the experimental Stokes parameters.

As discussed in [33], for input RCP on QW-q-plates, the output beam is a coherent superposition of RCP and LCP with a relative phase shift of $-\pi/2$ and a helical phase only in the LCP component. Hence, the interference yields a local linear polarization that rotates with the azimuth as $q\theta$. Such local linearly polarized states and their orientation with the azimuth are observed in the polarization map of Figure 9b,c. Note how these linear states rotate a value θ in panel (b) and half-θ in panel (c). Therefore, the output is a slanted pseudo-vector beam (hybrid vector beam) of order $\ell = q$. Therefore, the experimental polarization map of the CVBs show the good performance of both kind of devices.

5. Conclusions

We apply an imaging polarimetry-based approach to verify the homogeneity of a segmented radial polarizer and two continuous liquid-crystal q-plate retarders through the decomposition of their Mueller matrices and the calculation of the diattenuation, polarizance, depolarization, and retardance parameters. The space-variant orientation of the transmission axis of the radial polarizer and the optical axis of the q-plates were also obtained. It is important to know the quality of these commercial polarizing elements that generate vector beams. Our polarimetry system employs a polarization state generator based on liquid-crystal variable retarders and a polarimetric camera with a movable QWP as a polarization state analyzer. Although our experimental setup was not the most optimal due to the use of this movable QWP, the numerical and the experimental results were consistent. The results provided the interest of polarimetric methods to characterize vector beams generator systems with easy means, which could be implemented for real-time systems. In particular, it could be useful for testing new q-plate designs, like modal q-plates and meta q-plates, featuring arbitrary space-variant optical axes [44–46] and space-variant retardance [45]. Note that this type of studies would be useful for the quality control of these elements, obtaining larger standard deviations in the presence of manufacturing errors or surface scratches.

Author Contributions: Conceptualization, G.L.-M., M.d.M.S.-L., and I.M.; Methodology, Á.L. and J.C.; Software, G.L.-M.; Experimental validation, G.L.-M. and Á.L.; Formal analysis and data curation, G.L.-M.; Visualization, G.L.-M. and M.d.M.S.-L.; Writing—original draft preparation, G.L.-M., M.d.M.S.-L., and Á.L.; Writing—review and editing, all authors; Supervision, M.d.M.S.-L. and I.M.; Funding acquisition, I.M., M.d.M.S.-L., Á.L., and J.C. Project administration, I.M. and J.C. All authors have read and agreed to the published version of the manuscript.

Funding: This research was funded by Generalitat Valenciana, Conselleria d'Educació, Investigació, Cultura i Esport (grant PROMETEO-2017-154) and by Ministerio de Ciencia, Innovación y Universidades, Spain (grants RTI2018-097107-B-C31 and RTI2018-097107-B-C33).

Conflicts of Interest: The authors declare no conflict of interest.

Appendix A

This Appendix provides a summary of the Lu-Chipman decomposition [27]. Let us consider $\mathbf{M}$ as the measured MM. It can be written as $\mathbf{M} = \mathbf{M}_\Delta \cdot \mathbf{M}_R \cdot \mathbf{M}_D$. First, $\mathbf{M}$ is written as

$$\mathbf{M} = \begin{bmatrix} m_{00} & m_{01} & m_{02} & m_{03} \\ m_{10} & m_{11} & m_{12} & m_{13} \\ m_{20} & m_{21} & m_{22} & m_{23} \\ m_{30} & m_{31} & m_{32} & m_{33} \end{bmatrix} = m_{00} \begin{bmatrix} 1 & \vec{\mathbf{D}}^T \\ \vec{\mathbf{P}} & \mathbf{m} \end{bmatrix}, \tag{A1}$$

where $\vec{\mathbf{D}} = (1/m_{00})[m_{01}\, m_{02}\, m_{03}]^T$ and $\vec{\mathbf{P}} = (1/m_{00})[m_{10}\, m_{20}\, m_{30}]^T$ are the diattenuation and polarizance vectors, respectively, and $\mathbf{m}$ is the normalized 3×3 submatrix. The diattenuation (D) and polarizance (P) parameters are respectively given by

$$D = \left|\vec{\mathbf{D}}\right| = \frac{1}{m_{00}} \sqrt{m_{10}^2 + m_{20}^2 + m_{30}^2}, \text{ and } P = \left|\vec{\mathbf{P}}\right| = \frac{1}{m_{00}} \sqrt{m_{01}^2 + m_{02}^2 + m_{03}^2}. \tag{A2}$$

D characterizes the dependence of the sample transmission on the incident light polarization and P describes the sample capability to polarize unpolarized incident light.

Then, the diattenuation matrix $\mathbf{M}_D$ is determined as:

$$\mathbf{M}_D = m_{00} \begin{bmatrix} 1 & \vec{\mathbf{D}}^T \\ \vec{\mathbf{D}} & \mathbf{m}_D \end{bmatrix} \tag{A3}$$

where $\mathbf{m}_D = \sqrt{1-D^2}\mathbf{I} + \left(1-\sqrt{1-D^2}\right)\mathbf{D}\mathbf{D}^{\mathbf{T}}$, $\mathbf{I}$ is the 3×3 identity matrix, and $\widehat{\mathbf{D}} = \vec{\mathbf{D}}/D$ is the unitary vector along $\vec{\mathbf{D}}$. Once the diattenuation matrix $\mathbf{M}_D$ is calculated, the procedure to calculate the depolarization and retarder parameters depends on the singularity of $\mathbf{M}_D$. In our case of study, the diattenuation matrix of the radial polarizer is a singular matrix, and it is a non-singular matrix when dealing with the *q*-plate. Therefore, two different approaches must be followed in each case.

Appendix A.1. Case of a Singular Diattenuation Matrix

When $\mathbf{M}_D$ is a singular matrix, the decomposition of $\mathbf{M}$ given by [27]

$$\mathbf{M} = m_{00}\begin{bmatrix} 1 & \vec{\mathbf{D}}^T \\ \vec{\mathbf{P}} & \vec{\mathbf{P}}\vec{\mathbf{D}}^T \end{bmatrix} = \begin{bmatrix} 1 & \vec{0}^T \\ \vec{0} & P\mathbf{I} \end{bmatrix} \cdot \mathbf{M}_R \cdot m_{00}\begin{bmatrix} 1 & \vec{\mathbf{D}}^T \\ \vec{\mathbf{D}} & \vec{\mathbf{D}}\vec{\mathbf{D}}^T \end{bmatrix} \tag{A4}$$

The retarder and depolarizer matrices are not unique, therefore, the retarder matrix $\mathbf{M}_R$ is chosen following the criterion given in [24]. The retardance parameter is then calculated as

$$R = \left|\vec{\mathbf{R}}\right|, \text{ with } \vec{\mathbf{R}} = \frac{\widehat{\mathbf{P}} \times \vec{\mathbf{D}}}{\left|\widehat{\mathbf{P}} \times \vec{\mathbf{D}}\right|} \arccos\left(\widehat{\mathbf{P}} \cdot \vec{\mathbf{D}}\right), \tag{A5}$$

$\vec{\mathbf{R}}$ being the retardance vector, which includes the combined effect of linear and circular birefringence of the sample. Here, $\widehat{\mathbf{P}} = \vec{\mathbf{P}}/\left|\vec{\mathbf{P}}\right|$ is the unit vector along $\vec{\mathbf{P}}$.

The depolarization parameter is defined as [27]

$$\Delta = 1 - \left|\vec{\mathbf{P}}\right|. \tag{A6}$$

Finally, the orientation of the polarizer transmission axis (θ_{TA}) with respect to the horizontal axis is obtained from the elements of the diattenuation vector $\vec{\mathbf{D}}$ as [27]

$$\theta_{TA} = \frac{1}{2}\arctan\left(\frac{m_{02}}{m_{01}}\right). \tag{A7}$$

Appendix A.2. Case of a Non-Singular Diattenuation Matrix

On the other hand, when the diattenuation matrix $\mathbf{M}_D$ is not a singular matrix (as is the case for the *q*-plates) its inverse matrix can be calculated as [29]

$$\mathbf{M}_D^{-1} = \frac{1}{a^2}\begin{bmatrix} 1 & -\vec{\mathbf{D}}^T \\ -\vec{\mathbf{D}} & \mathbf{I} \end{bmatrix} + \frac{1}{a^2(a+1)}\begin{bmatrix} 0 & \vec{0}^T \\ \vec{0} & \vec{\mathbf{D}}\vec{\mathbf{D}}^T \end{bmatrix}, \tag{A8}$$

where $a = \sqrt{1-D^2}$. Then, matrices $\mathbf{M}_\Delta$ and $\mathbf{M}_R$ can be calculated from matrix $\mathbf{M}' = \mathbf{M}\mathbf{M}_D^{-1} = \mathbf{M}_\Delta\mathbf{M}_R$, which can be expanded to read as:

$$\mathbf{M}' = \mathbf{M}_\Delta\mathbf{M}_R = \begin{bmatrix} 1 & \vec{0}^T \\ \vec{\mathbf{P}}_\Delta & \mathbf{m}_\Delta \end{bmatrix} \cdot \begin{bmatrix} 1 & \vec{0}^T \\ \vec{0} & \mathbf{m}_R \end{bmatrix} = \begin{bmatrix} 1 & \vec{0}^T \\ \vec{\mathbf{P}}_\Delta & \mathbf{m}_\Delta\mathbf{m}_R \end{bmatrix}, \tag{A9}$$

where $\vec{\mathbf{P}}_\Delta = (\vec{\mathbf{P}} - \mathbf{m} \cdot \vec{\mathbf{D}})/(1-D^2)$ denotes the polarizance vector of the depolarizer, and $\mathbf{m}_\Delta$ and $\mathbf{m}_R$ are 3×3 sub-matrices of $\mathbf{M}_\Delta$ and $\mathbf{M}_R$.

Let us consider $\mathbf{m'} = \mathbf{m}_\Delta \mathbf{m}_R$ and let $\lambda_1, \lambda_2, \lambda_3$ be the eigenvalues of $\mathbf{m'}(\mathbf{m'})^T$. Then, $\mathbf{m}_\Delta$ m_Δ is defined by

$$\mathbf{m}_\Delta = \pm\Big[\mathbf{m'}(\mathbf{m'})^T + \Big(\sqrt{\lambda_1\lambda_2} + \sqrt{\lambda_2\lambda_3} + \sqrt{\lambda_1\lambda_3}\Big)\mathbf{I}\Big]^{-1}\Big[\Big(\sqrt{\lambda_1} + \sqrt{\lambda_2} + \sqrt{\lambda_3}\Big)\mathbf{m'}(\mathbf{m'})^T + \sqrt{\lambda_1\lambda_2\lambda_3}\mathbf{I}\Big], \tag{A10}$$

the sign being positive if $\det(\mathbf{m'}) > 0$ and negative if $\det(\mathbf{m'}) < 0$. Knowing $\vec{\mathbf{P}}_\Delta$ and $\mathbf{m}_\Delta$ determines $\mathbf{M}_\Delta$, and the depolarization parameter Δ is then defined through its diagonal elements as

$$\Delta = 1 - \frac{1}{3}\big|\mathrm{tr}(\mathbf{M}_\Delta) - 1\big|,\ 0 \le \Delta \le 1. \tag{A11}$$

Finally, the retarder matrix $\mathbf{M}_R$. is obtained from Equation (A9) as $\mathbf{M}_R = \mathbf{M}_\Delta^{-1}\mathbf{M'}$, and the retardance parameter (R) is calculated by

$$R = \arccos\left(\frac{1}{2}\mathrm{tr}(\mathbf{M}_R) - 1\right),\ 0 \le R \le \pi. \tag{A12a}$$

$$R = 2\pi - \arccos\left(\frac{1}{2}\mathrm{tr}(\mathbf{M}_R) - 1\right),\ \pi \le R \le 2\pi. \tag{A12b}$$

The retardance vector $\vec{\mathbf{R}}$ is found from the elements M_{Rij} of the matrix $\mathbf{M}_R$ as [29]

$$\vec{\mathbf{R}} = \begin{bmatrix} R_1 \\ R_2 \\ R_3 \end{bmatrix} = \frac{R}{2\sin R}\begin{bmatrix} M_{R23} - M_{R32} \\ M_{R31} - M_{R13} \\ M_{R12} - M_{R21} \end{bmatrix}, \tag{A13}$$

and the orientation of the retarder optical axis (θ_{OA}) is calculated as

$$\theta_{OA} = \frac{1}{2}\arctan\left(\frac{R_2}{R_1}\right). \tag{A14}$$

References

1. Beeckman, J.; Neyts, K.; Vanbrabant, P.J.M. Liquid-crystal photonic applications. *Opt. Eng.* **2011**, *50*, 081202. [CrossRef]
2. Bueno, J.M. Polarimetry using liquid-crystal variable retarders: Theory and calibration. *J. Opt. A Pure Appl. Opt.* **2000**, *2*, 216–222. [CrossRef]
3. Uribe-Patarroyo, N.; Alvarez-Herrero, A.; Heredero, R.L.; Iniesta, J.C.D.T.; Jiménez, A.C.L.; Domingo, V.; Gasent, J.L.; Jochum, L.; Pillet, V.M. IMaX: A polarimeter based on Liquid Crystal Variable Retarders for an aerospace mission. *Phys. Status Solidi* **2008**, *5*, 1041–1045. [CrossRef]
4. Tyo, J.S.; Goldstein, D.L.; Chenault, D.B.; Shaw, J.A. Review of passive imaging polarimetry for remote sensing applications. *Appl. Opt.* **2006**, *45*, 5453–5469. [CrossRef] [PubMed]
5. Lizana, A.; Foldyna, M.; Stchakovsky, M.; Georges, B.; Nicolas, D.; Garcia-Caurel, E. Enhanced sensitivity to dielectric function and thickness of absorbing thin films by combining total internal reflection ellipsometry with standard ellipsometry and reflectometry. *J. Phys. D Appl. Phys.* **2013**, *46*, 105501. [CrossRef]
6. Lizana, A.; Van Eeckhout, A.; Adamczyk, K.; Rodríguez, C.; Escalera, J.C.; Garcia-Caurel, E.; Moreno, I.; Campos, J. Polarization gating based on Mueller matrices. *J. Biomed. Opt.* **2017**, *22*, 056004. [CrossRef]
7. Bueno, J.M.; Hunter, J.J.; Cookson, C.J.; Kisilak, M.L.; Campbell, M.C.W. Improved scanning laser fundus imaging using polarimetry. *J. Opt. Soc. Am. A* **2007**, *24*, 1337–1348. [CrossRef]
8. Wolfe, J.E.; Chipman, R.A. Polarimetric characterization of liquid-crystal-on-silicon panels. *Appl. Opt.* **2006**, *45*, 1688–1703. [CrossRef]
9. Lizana, A.; Moreno, I.; Iemmi, C.; Márquez, A.; Campos, J.; Yzuel, M. Time-resolved Mueller matrix analysis of a liquid crystal on silicon display. *Appl. Opt.* **2008**, *47*, 4267–4274. [CrossRef]

10. Ding, Z.; Yao, Y.; Yao, X.S.; Chen, X.; Wang, C.; Wang, S.; Liu, T. Demonstration of Compact In situ Mueller-Matrix Polarimetry Based on Binary Polarization Rotators. *IEEE Access* **2019**, *7*, 144561–144571. [CrossRef]
11. Parejo, P.G.; Campos-Jara, A.; Garcia-Caurel, E.; Arteaga, O.; Alvarez-Herrero, A. Nonideal optical response of liquid crystal variable retarders and its impact on their performance as polarization modulators. *J. Vac. Sci. Technol. B* **2020**, *38*, 014009. [CrossRef]
12. Marc, P.; Bennis, N.; Spadlo, A.; Kalbarczyk, A.; Węgłowski, R.; Garbat, K.; Jaroszewicz, L.R. Monochromatic Depolarizer Based on Liquid Crystal. *Crystals* **2019**, *9*, 387. [CrossRef]
13. Rosales-Guzmán, C.; Ndagano, B.; Forbes, A. A review of complex vector light fields and their applications. *J. Opt.* **2018**, *20*, 123001. [CrossRef]
14. Zhan, Q. Cylindrical vector beams: From mathematical concepts to applications. *Adv. Opt. Photonics* **2009**, *1*, 1–57. [CrossRef]
15. Pachava, S.; Dharmavarapu, R.; Anand, V.; Jayakumar, S.; Manthalkar, A.; Dixit, A.; Viswanathan, N.K.; Srinivasan, B.; Bhattacharya, S. Generation and decomposition of scalar and vector modes carrying orbital angular momentum: A review. *Opt. Eng.* **2019**, *59*, 041205. [CrossRef]
16. De Sande, J.C.G.; De Sande, J.C.G.; Santarsiero, M.; Piquero, G. Mueller matrix polarimetry using full Poincaré beams. *Opt. Lasers Eng.* **2019**, *122*, 134–141. [CrossRef]
17. Zhao, B.; Hu, X.-B.; Rodriguez-Fajardo, V.; Zhu, Z.-H.; Gao, W.; Forbes, A.; Rosales-Guzmán, C. Real-time Stokes polarimetry using a digital micromirror device. *Opt. Express* **2019**, *27*, 31087–31093. [CrossRef]
18. Stalder, M.; Schadt, M. Linearly polarized light with axial symmetry generated by liquid-crystal polarization converters. *Opt. Lett.* **1996**, *21*, 1948–1950. [CrossRef]
19. Rubano, A.; Cardano, F.; Piccirillo, B.; Marrucci, L. Q-plate technology: A progress review. *J. Opt. Soc. Am. B* **2019**, *36*, D70–D87. [CrossRef]
20. Cardano, F.; Karimi, E.; Slussarenko, S.; Marrucci, L.; De Lisio, C.; Santamato, E. Polarization pattern of vector vortex beams generated by *q*-plates with different topological charges. *Appl. Opt.* **2012**, *51*, C1–C6. [CrossRef]
21. Nersisyan, S.; Tabiryan, N.; Steeves, D.M.; Kimball, B.R. Fabrication of liquid crystal polymer axial waveplates for UV-IR wavelengths. *Opt. Express* **2009**, *17*, 11926–11934. [CrossRef] [PubMed]
22. Beresna, M.; Gecevičius, M.; Kazansky, P.G.; Gertus, T. Radially polarized optical vortex converter created by femtosecond laser nanostructuring of glass. *Appl. Phys. Lett.* **2011**, *98*, 201101. [CrossRef]
23. Sánchez-López, M.M.; Moreno, I.; Davis, J.A.; Puerto-Garcia, D.; Abella, I.; Delaney, S.W. Extending the use of commercial *q*-plates for the generation of high-order and hybrid vector beams. *Laser Beam Shap. XVIII* **2018**, *10744*, 1074407. [CrossRef]
24. Badham, K.; Delaney, S.; Hashimotono, N.; Sánchez-López, M.M.; Kurihara, M.; Tanabe, A.; Moreno, I.; Davis, J.A. Generation of vector beams at 1550 nm telecommunications wavelength using a segmented q -plate. *Opt. Eng.* **2016**, *55*, 30502. [CrossRef]
25. Quiceno-Moreno, J.C.; Marco, D.; Sánchez-López, M.M.; Solarte, E.; Moreno, I. Analysis of Hybrid Vector Beams Generated with a Detuned Q-Plate. *Appl. Sci.* **2020**, *10*, 3427. [CrossRef]
26. Moreno, I.; Albero, J.; Davis, J.A.; Cottrell, D.M.; Cushing, J.B. Polarization manipulation of radially polarized beams. *Opt. Eng.* **2012**, *51*, 128003. [CrossRef]
27. Lu, S.-Y.; Chipman, R.A. Interpretation of Mueller matrices based on polar decomposition. *J. Opt. Soc. Am. A* **1996**, *13*, 1106–1113. [CrossRef]
28. Morales, G.L.; Sánchez-López, M.D.M.; Soriano, I.M. Liquid-crystal polarization state generator. In Proceedings of the Unconventional Optical Imaging II, Online. Strasbourg, France, 7–10 April 2020; p. 11351. [CrossRef]
29. Goldstein, D.H. *Polarized Light*; Marcel Dekker: New York, NY, USA, 2010.
30. CODIXX. Available online: https://www.codixx.de/en/colorpol-s-patterned/colorpol-s-patterned-polarizer.html (accessed on 2 November 2020).
31. THORLABS. Available online: https://www.thorlabs.com/newgrouppage9.cfm?objectgroup_id=9098 (accessed on 2 November 2020).
32. Marco, D.; Sánchez-López, M.M.; García-Martínez, P.; Moreno, I. Using birefringence colors to evaluate a tunable liquid-crystal q-plate. *J. Opt. Soc. Am. B* **2019**, *36*, D34–D41. [CrossRef]

33. Sánchez-López, M.M.; Abella, I.; Puerto-García, D.; Davis, J.A.; Moreno, I. Spectral performance of a zero-order liquid-crystal polymer commercial q-plate for the generation of vector beams at different wavelengths. *Opt. Laser Technol.* **2018**, *106*, 168–176. [CrossRef]
34. Morio, J.; Goudail, F. Influence of the order of diattenuator, retarder, and polarizer in polar decomposition of Mueller matrices. *Opt. Lett.* **2004**, *29*, 2234–2236. [CrossRef]
35. Ossikovski, R.; De Martino, A.; Guyot, S. Forward and reverse product decompositions of depolarizing Mueller matrices. *Opt. Lett.* **2007**, *32*, 689–691. [CrossRef] [PubMed]
36. ArcOptix. Variable Phase Retarder. Available online: http://www.arcoptix.com/variable_phase_retarder.htm (accessed on 2 November 2020).
37. Hinds Instruments. Mueller Polarimeters. Available online: https://www.hindsinstruments.com/products/polarimeters/mueller-polarimeter/ (accessed on 4 December 2020).
38. Espinosa-Luna, R.; Zhan, Q. Polarization and Polarizing Optical Devices. In *Fundamentals and Basic Optical Instruments, Handbook of Optical Engineering*; CRC Press: New York, NY, USA, 2017.
39. Vargas, J.; Uribe-Patarroyo, N.; Quiroga, J.A.; Alvarez-Herrero, A.; Belenguer, T. Optical inspection of liquid crystal variable retarder inhomogeneities. *Appl. Opt.* **2010**, *49*, 568–574. [CrossRef] [PubMed]
40. Moallemi, P.; Behnampourii, M. Adaptive optimum notch filter for periodic noise reduction in digital images. *AUT J. Electr. Eng.* **2010**, *42*, 1–7.
41. Smith, M.H.; Woodruff, J.B.; Howe, J.D. Beam wander considerations in imaging polarimetry. In Proceedings of the SPIE's International Symposium on Optical Science, Engineering, and Instrumentation, Denver, CO, USA, 18–23 July 1999; Volume 3754, pp. 50–54. [CrossRef]
42. Gil, J.J.; Ossikovski, R. *Polarized Light and the Mueller Matrix Approach*; CRC Press: Boca Raton, FL, USA, 2016.
43. Ju, H.; Ren, L.; Liang, J.; Qu, E.; Bai, Z. Method for Mueller matrix acquisition based on a division-of-aperture simultaneous polarimetric imaging technique. *J. Quant. Spectrosc. Radiat. Transf.* **2019**, *225*, 39–44. [CrossRef]
44. Ji, W.; Lee, C.-H.; Chen, P.; Hu, W.; Ming, Y.; Zhang, L.; Lin, T.-H.; Chigrinov, V.G.; Lu, Y.-Q. Meta-q-plate for complex beam shaping. *Sci. Rep.* **2016**, *6*, 25528. [CrossRef]
45. Rafayelyan, M.; Brasselet, E. Laguerre–Gaussian modal *q*-plates. *Opt. Lett.* **2017**, *42*, 1966–1969. [CrossRef]
46. Holland, J.E.; Moreno, I.; Davis, J.A.; Sánchez-López, M.M.; Cottrell, D.M. Q-plates with a nonlinear azimuthal distribution of the principal axis: Application to encoding binary data. *Appl. Opt.* **2018**, *57*, 1005–1010. [CrossRef]